Potential use of lightweight aggregate (LWA) produced from bottom coal ash for internal curing of concrete systems

Potential Use of Lightweight Aggregate (LWA) Produced from Bottom Coal Ash for Internal Curing of Concrete Systems

Mohammad Balapour[1], Weijin Zhao[1], E.J. Garboczi[2], Nay Ye Oo[1], Sabrina Spatari[1], Y. Grace Hsuan[1], Pieter Billen[3], Yaghoob Farnam[1]

[1]Drexel University, Department of Civil, Architectural and Environmental Engineering, 3141 Chestnut Street, Philadelphia, PA 19104, United States

[2]National Institute of Standards and Technology, Applied Chemicals and Materials Division, Boulder, CO 80305, United States

[3]University of Antwerp, BioGEM, Salesianenlaan 90, 2660 Hoboken, Belgium

Abstract

This study evaluates the potential use of a novel lightweight aggregate (LWA), spherical porous reactive aggregate (SPoRA), produced from waste coal bottom ash, for internal curing of concrete. The engineering properties of SPoRA required for concrete internal curing were assessed including specific gravity, porosity, sphericity, water absorption, and water desorption. SPoRA showed a low oven dry specific gravity, ranging from 0.83 to 1.43, accompanied by high porosity which makes it capable of storing the amount of water needed for concrete internal curing. Through X-ray computed tomography (XCT), the high porosity of SPoRA (39.6 % to 57.8 %, by volume) was measured and confirmed, and its sphericity, which influences the workability of concrete, was evaluated. XCT evaluation also showed that the pore structure of SPoRA is well connected, allowing stored water to move through the pore structure to the outer surface during the self-desiccation of concrete. SPoRA's 72 h water absorption not only passed the requirements of ASTM C1761 for internal curing (water absorption > 5 % and minimum of 85 % water desorption at 94 % relative humidity, RH), but also showed superior performance in comparison to LWAs available in the market, which were also evaluated in this study. Moreover, the SPoRA desorption

isotherms showed its capability for releasing a favorable amount of absorbed water as the internal RH decreases during concrete self-desiccation, thereby providing promising desorption behavior for concrete internal curing and can be a promising LWA for internal curing of concrete.

Keywords: Concrete, Lightweight Aggregate, Internal Curing, Pore Structure, Sintering, Sorption Properties.

1. Introduction

Curing is an essential process for concrete. Proper curing enables the cement to hydrate and develop its potential strength and durability. Traditional methods for curing concrete involve applying external water or curing compounds, neither of which sufficiently penetrate the entire depth to completely cure the concrete [1,2]. In these cases, where the moisture transport properties in concrete limit the external water penetrating to the core of the concrete, the internal relative humidity (RH) can drop low enough to cease the hydration inside the concrete (self-dessication). Methods such as internal curing have been recommended to increase curing efficiency in concrete [3]. For internal curing, an internal medium that stores a sufficient amount of water is added to the concrete, so that the stored water can gradually release over time to maintain a desirable internal RH that maintains curing internally. The use of lightweight aggregate (LWA) (i.e., porous aggregate) in concrete is a promising method to effectively improve concrete curing [3–5]. For internal curing, LWAs need to possess necessary engineering properties including low specific gravity, high water absorption capacity, and a connected pore structure that enables water to effectively absorb, from the outside to the inside during mixing, and desorb from the inside to the outside of the LWA during concrete self-dessication [6–9]. While these material properties are critical factors for internal curing, the negative effects of incorporating LWA on the mechanical

properties of concrete, due to the lower stiffness and strength of porous aggregates compared to non-porous aggregates, can be managed by concrete mixture design modifications [3,10].

Accessibility to LWAs for internal curing is becoming increasingly challenging in the United States (US) due to limited availability in many regions, increasing market demands, costs, and environmental issues [11]. Accordingly, alternative sustainable methods are needed to produce LWAs for internal curing [11,12]. One method to produce LWAs is the use of coal combustion products (CCP) or coal ash [13–15]. Every year, a substantial amount of CCP residues, including fly ash, bottom ash, boiler slag, fluidized bed combustion ash, and flue gas, are generated during the combustion of coal in many power plants around the country [15] that have historically led to a large stock of unused coal ash.

Fly ash and bottom ash have been reported as appropriate raw materials for producing LWA due to the formation of a vitreous phase followed by expansion and creation of porosity at elevated temperature [11,14,16]. Both types of ashes possess essentially similar elemental constituents, but their average particle size and shape are different. Bottom ash particles are large in size, mainly ranging from 150 μm to 20 mm [17], irregular in shape and contain more pores/cavities, compared to fly ash particles, which are small (≈ 20 μm) and more spherical [13]. Bijen reviewed alternative modes of manufacturing LWA made from fly ash [18]. One process includes mixing of raw materials, agglomeration, and hardening. Agglomeration techniques consist of agitation, granulation, and compacting. Hardening, involving sintering, autoclaving and cold bonding, was introduced. The sintering was found to be acceptable for a high carbon content fly ash, while autoclaved and cold bonded pellets were found to be preferable for low carbon fly ash [18]. Verma et al. [19] examined the use of fly ash blended with water and clay soil as binders to enhance the cohesion of pelletized nodules for the LWA sintering process between 1050 °C and 1200 °C. The

LWA produced had an oven-dry specific gravity of 1.23 and water absorption ranging from 15 % to 20 %. Zorić et al. [20] used fly ash, waste glass, and carboxyl methyl cellulose (CMC) as raw materials for production of LWA. Waste glass powder was used to provide a slag phase during the sintering procedure, while the CMC was a blowing agent for generating pores. The LWA was sintered at 1150 °C and had a 24 h water absorption of 42.7 %. In studies by Bethanis et al. [21] and Cheeseman et al. [22], bottom ash was used as a raw material to produce LWA. Bethanis et al. [21] used a temperature range between 1020 °C and 1100 °C for the sintering process and a residence time of 1 h at the maximum temperature. They observed reductions in LWA water absorption as sintering temperature increased because of reductions in the connected and water-accessible pores. Cheeseman et al. [22] added a controlled amount of water into the milled powder to produce identical 8 mm to 10 mm spherical pellets. The aggregates sintered at 1000 °C to 1050 °C had average densities ranging from 1.4 g/cm^3 to 1.6 g/cm^3 with a water absorption value near 10 %. Karayannis et al. [23] utilized fly ash and bottom ash as their raw materials, where the fly ash had a much higher CaO content than bottom ash, but had less residual carbon. They prepared green pellets (prior to sintering) with 13 mm diameter using a stainless-steel die, and applied pressure using a hydraulic press during pelletization. They used two-step sintering, where the temperature first reached 1150 °C, then was rapidly cooled to 950 °C and was held isothermally for 2 h or 4 h. The advantages of this two-step sintering process were reported to be: (1) obtaining more pronounced crystallinity from the fly ash and bottom ash and (2) forming finer microstructures and more interconnected porosity [23].

While processes in which LWAs can be made using CCP have been documented in the literature, the main goal of this study is to evaluate the potential use of a novel LWA, spherical porous reactive aggregate (SPoRA) produced from waste bottom ash, for internal curing of concrete.

SPoRA possesses three main features that make it a unique LWA in comparison to traditional LWAs: a spherical shape to increase the workability of concrete, a porous structure that can absorb and desorb water for internal curing, and a glassy surface (with crystalline internal structure) that can enable surface reactivity with cementitious phases in concrete, ensuring a better bond with the cement paste matrix [24]. Previous works [24,25] have shown that SPoRA can be successfully produced from bottom ash through a sintering process. This paper extends this earlier work and the main objective of this paper is to evaluate the engineering properties of SPoRA that are required for internal curing of concrete. Engineering properties important to LWAs, including porosity, sphericity, specific gravity, water absorption, and water desorption, were measured to evaluate whether SPoRA can serve as an LWA that is efficient for concrete internal curing. The pore structure, porosity and sphericity of SPoRA were characterized using X-ray computed tomography (XCT). Time dependent water absorption was measured to evaluate SPoRA's capability in storing a sufficient amount of water for cement hydration in its pore structure. Water desorption behavior of SpoRA was characterized using a vapor sorption analyzer (VSA) to evaluate SPoRA's capability in releasing a promising portion of the stored water from its pore structure to help cement hydration to continue inside the concrete.

2. Experimental program

2.1 Materials

Two types of bottom ash were used in this study to produce SPoRA: (1) high-calcium content ash, denoted by WP, and (2) low-calcium content ash, denoted by NV. The oxide compositions were measured by a Bruker S8 Tiger Wavelength Dispersive X-ray Fluorescence[1*] instrument by the

[*] Certain commercial equipment, software and/or materials are identified in this paper in order to adequately specify the experimental procedure. In no case does such identification imply recommendation or endorsement by the National Institute of Standards and Technology, nor does it imply that the equipment and/or materials used are necessarily the best available for the purpose.

bottom ash vendor according to ASTM D4326–13 [26] and are provided in Table 1. The crystalline phases were detected by X-ray diffraction (XRD) using a Bruker D2 PHASER with Cu radiation. The observed and calculated spectra (obtained with the Rietveld refinement method) are shown in Figure 1. The main NV mineral components were quartz, mullite, calcite, vaterite, and hematite. For the WP ash, the detected minerals included quartz, mullite, calcite, gehlenite, lime, and $CaAl_2O_4$. A stronger peak corresponding to quartz was observed in NV in comparison to WP, which is consistent with the higher SiO_2 content (see Table 1), whereas considerable amounts of calcite and lime were found in WP as reflected by a higher calcium (CaO) content in WP than NV.

Table 1. Oxide compositions of NV and WP ashes used in this study [24]

Chemical Composition (% by mass)	**Sample Name**	
	NV	**WP**
SiO_2	63.2	43.1
Al_2O_3	20.1	17.1
Fe_2O_3	6.66	7.29
SO_3	0.39	0.64
CaO	3.51	22.5
Na_2O	1.43	1.19
MgO	0.97	4.10
K_2O	1.13	0.41
P_2O_5	0.09	0.91
TiO_2	1.03	1.25
Total	98.53	98.52

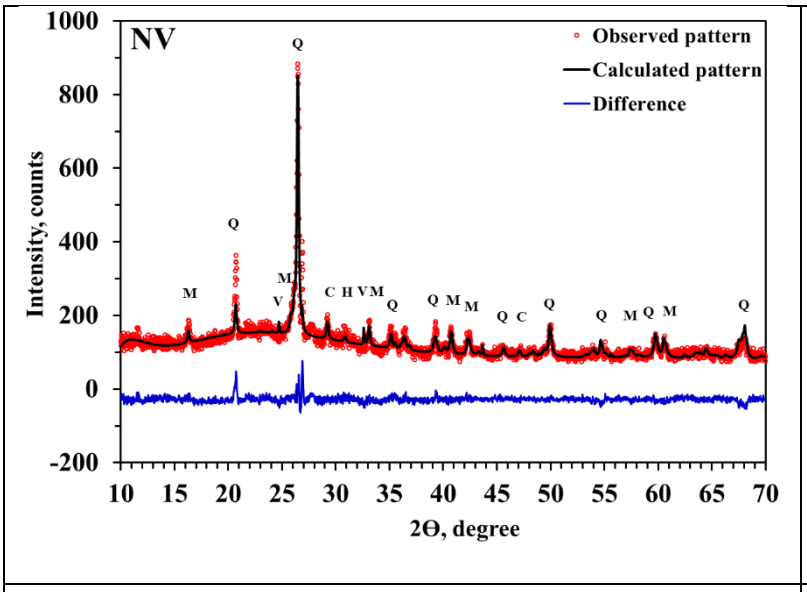

NV

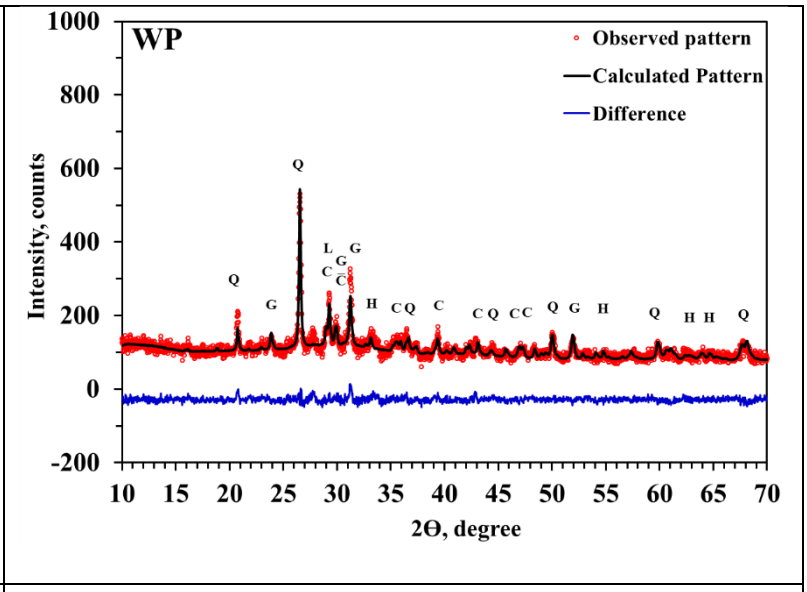

WP

Figure 1. XRD spectra of NV and WP ash. Quartz=Q, Mullite=M, Calcite=C, Vaterite=V, Hematite=H, Gehlenite=G, Lime=L and $CaAl_2O_4$=$\bar{C}$.

2.2 SPoRA preparation procedure

A five-step process [24] was used to produce the SPoRA. In Step 1, the moisture of the bottom ash was removed in an oven at a temperature of 110 °C ± 5 °C until the mass of the ash reached a constant value. After drying, mechanical sieving (step 2) was used to divide the ash into five size ranges, which were then blended in amounts that followed the Fuller equation (Equation 1):

$$\boldsymbol{P_i = \left(\frac{d_i}{D}\right)^n \times 100\%} \qquad \text{Equation 1}$$

where:

P_i = Percent by mass passing the i^{th} sieve

d_i = Opening size of the i^{th} sieve, μm

D = Maximum particle size, μm

n = Fuller exponent

The maximum particle size chosen was 600 μm (i.e., all particles passed the #30 or 600 μm sieve), since pellets could not be produced with larger particles. The value of n was selected to be 0.5 in order to maximize the packing density [27].

In Step 3, the blended ash was mixed with NaOH aqueous solutions (2.5 mol/L, 6.25 mol/L and 10 mol/L) to give mass concentrations (mass of solid NaOH per mass of bottom ash) of 4 %, 10 %, and 16 % at a liquid/solid (L/S) ratio of 0.4. The wet mixes were then compacted into a spherical pellet (green pellet) with a diameter of 16 mm using a plastic mold and a compressive load of 18.77 N. NaOH was added as a fluxing agent to lower the melting temperature of the ashes as well as to reduce the viscosity of their molten phase. The NaOH addition was also found to chemically bind bottom ashes by initiating geopolymerization, which helped to retain the spherical shape of the green pellets before the sintering process. Samples were made to be spherical since spheres provide the minimum aggregate surface area that not only can improve concrete workability, but also can result in lower paste and cement demand in the concrete mixture. The L/S ratio of 0.4 was found to provide the best dry integrity (cohesion of particles) for green pellets. After demolding the green pellets, moisture was removed in Step 4 by placing the green pellets in a controlled environmental chamber at 40 °C and 30 % RH for 30 h. Finally, in Step 5, the pellets were sintered in a tube furnace at a temperature of 1160 °C. Residence times of 4 min and 8 min were used,

followed by immediate natural cooling to room temperature (23 °C). Table 2 shows the types of SPoRA prepared in this study. Aggregates are abbreviated by the following format: XX-X%-Xmin where XX represents bottom ash type (NV or WP), X% is the NaOH concentration (% by mass), and Xmin is sintering time (in min), respectively. For instance, WP-10%-8min indicates aggregates that are made from WP ash with 10 % NaOH concentration (by mass) and sintered for 8 min.

Table 2. SPoRA preparation matrix

Ash type	L/S	Residence time	NaOH concentration (%)			Code*
NV	0.4	4 min	4	10	16	NV-4%-4min
						NV-4%-8min
						NV-10%-4min
						NV-10%-8min
		8 min				NV-16%-4min
						NV-16%-8min
WP		4 min	4	10	16	WP-4%-4min
						WP-4%-8min
						WP-10%-4min
						WP-10%-8min
		8 min				WP-16%-4min
						WP-16%-8min

*For each aggregate type, at least three replicates were produced for further testing.

173

174 *2.3 Testing procedures*

175 *2.3.1 X-ray Computed Tomography (XCT)*

176 The porosity and pore structure, which influence density, absorption, and desorption properties of
177 the SPoRA, can be interpretted from data obtained from the XCT tests [28]. Moreover, a physical
178 shape parameter, such as the sphericity index, can be calculated using XCT data [29]. The XCT
179 test was performed using a Zeiss Versa XRM 500 system. XCT is a non-destructive three-
180 dimensional imaging technique that captures 2D X-ray projections (radiographs) of a sample
181 (mounted to a stage) as the stage is rotating. A series of 2D projections were taken from each
182 SPoRA sample and stacked together to image the entire 3D sample volume [30]. The 2D
183 projections represent the difference in X-ray attenuation at each point, which depends on the
184 material density and average atomic number at that point. In the reconstructed images, solid voxels
185 appear brighter [31,32] while pores appear to be dark gray or black. The SPoRA images were taken
186 with voxels of edge length approximately 18 μm, with some variations among aggregates. The X-
187 ray source was set for 80 kV and 87 μA during imaging.

188 For each SPoRA sample, approximately 800 XCT stack images were obtained. Images were
189 analyzed by ImagePro Analyzer software [33][*]. The 16 bit 2D reconstructed slices that came
190 directly from the XCT instrument were first converted to 8 bit images, i.e., 0 to 255 grayscale
191 value (GSV), in order to reduce the computer memory requirement for image analysis.
192 Segmentation was then implemented to separate solid phases from pore phases. For segmentation,
193 a simple global thresholding method (generally different for each SPoRA) was used, in which a
194 single GSV threshold was selected based on image intensity histogram analysis. Voxels with GSV

less than the selected threshold were assigned to pores (GSV = 255) while voxels with GSV larger than the threshold were assigned to solid phases (GSV = 0)[31,34].

2.3.2 Specific gravity and sorption properties

The specific gravity and sorption properties of the SPoRA samples were measured. Additionally, three manufactured LWAs were evaluated as references for comparison. These three reference LWAs included two natural LWA samples (Sample A and Sample B) that are made from expanded shale, clay and slate (ESCS) and one foamed glass LWA produced from waste glass.

A buoyancy method was used according to ASTM C127 [35] to measure the specific gravity of the SPoRA samples. Oven dry (OD), saturated surface dry (SSD), and apparent specific gravity, which depends on the solid constituents and does not consider the pore space within the materials, were obtained. Additionally, the vacuum absorption capacity, which indicates the maximum possible absorption capacity of an aggregate, was measured. To obtain the OD mass, SPoRA samples were dried in an oven at a temperature of 110 °C ± 5 °C for a minimum of 12 h. OD samples were de-aerated with a vacuum pump (pressure of 1.33 kPa ± 0.33 kPa) for 3 h followed by introducing deionized water, which was previously de-aerated, to the samples under vacuum conditions. Samples continued to be de-aerated under vacuum for an additional 1 h. After vacuum saturation of the samples, the surface water was removed and the SSD mass was measured. Samples were then placed in the buoyancy container and the apparent mass was measured.

It is important to note that the water absorption in the SPoRA samples takes place over time; therefore, a Volumetric Flask method [10] was conducted separately on the OD samples to

evaluate the water absorption as a function of time. Water absorption was measured at intervals described in [10] up to 120 h.

2.3.2 Desorption properties

The effective desorption of water from saturated SPoRA samples over time is an essential parameter controlling the release of water for internal curing during concrete self-desiccation when the internal RH drops continuously during hydration. Accordingly, desorption isotherms were obtained for the SPoRA samples using a vapor sorption analyzer (VSA). The VSA was also performed on the reference LWAs. To prepare a VSA test specimen, the aggregate was first cut using a diamond saw into slices with thicknesses of 1 mm to 2 mm. Then a small piece (40 mg to 55 mg) was obtained by breaking the slice using twisters and placed in a VSA pan. The pan containing the specimen was suspended from the VSA balance (± 0.001 mg accuracy) and placed in the RH chamber to equilibrate, defined as the point where the mass change reaches a value less than 0.001 % per 15 min at 23.0 °C ± 0.05 °C and 98 % ± 0.1 % RH. Afterwards, the RH in the chamber was decreased in discrete intervals of 1 % RH to reach 80 % RH, allowing the sample to equilibrate at each interval (same definition of equilibrate). The chamber RH was then dropped to 0 % RH to fully remove all moisture from the specimen.

3. Results and discussion

3.1 Physical appearance

For each SPoRA sample described in Table 2, multiple replicates were produced. To evaluate the appearance and shape of SPoRA, high-quality photos were taken from different directions: top

view, where the direction of the photo was aligned with the gravitational direction of the pellet during the sintering process, and front view, where the direction of the photo was perpendicular to the gravitational direction of the pellet during the sintering process. The distance between the camera and the aggregate were kept constant during imaging to maintain the same magnification for all photos. Figure 2 and Figure 3 show representative images of SPoRA generated from NV and WP ashes, respectively. Various sample replicates possessed approximately the same physical appearance for each specific category of aggregates (considering ash type, NaOH concentration, and residence time); the representative images shown in Figure 2 and Figure 3 were selected to best illustrate the overall physical appearance of the SPoRA samples.

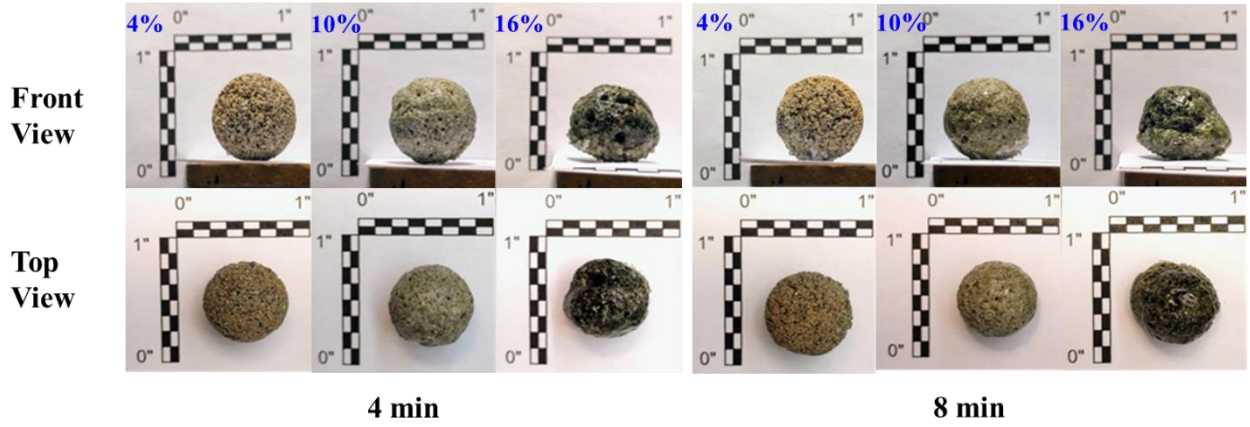

Figure 2. Front and top views of sintered NV at 1160 °C for 4 min and 8 min (the percentage in the upper left corner of each image is the NaOH concentration). The patterned bars show 25.4 mm (1 in).

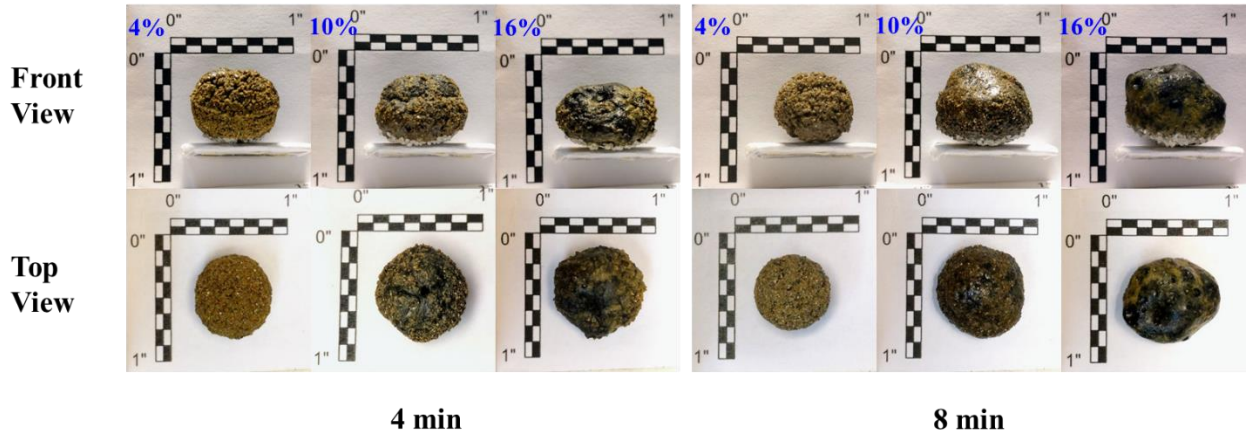

Figure 3. Front and top views of sintered WP at 1160 °C for 4 min and 8 min (the percentage in the upper left corner of each image is the NaOH concentration). The patterned bars show 25.4 mm (1 in).

For the NV aggregates, it was found that at NaOH concentration of 4 %, the aggregate does not deform during the sintering process. These SPoRAs appeared to be yellowish-brown in color with a granular texture surface. As the NaOH concentration increased to 10 %, the NV aggregate was still spherical, while the color changed to pale grey with a noticeably glassy surface. As the NaOH concentration increased to 16 %, the aggregate exhibited the greatest deformation as the amount of liquid molten phase increased during the sintering process [24]. Also, its color became dark grey and with a more pronouced glassy surface.

For the WP material, the aggregate started to deform at NaOH concentration higher than 4%, and the level of deformation increased as the NaOH concentration increased. While the surface of the 4% NaOH aggregate appeared to be granular and yellowish brown, it transformed to a smooth dark glassy surface for 10 % and 16 % NaOH.

Comparing the two types of aggregates at 4 % NaOH, the WP-4%-4min seemed to have a weaker bonding in comparison to NV-4%-4min as after sintering some particles fell off during handling. This can be attributed to the fact that no glassy surface formed on the WP-4%-4min aggregates, which would have helped maintain the integrity of the aggregate.

3.2 X-ray CT results

3.2.1 Cross-sectional binary images of SPoRA

The cross-sectional binary images of SPoRAs sintered for 4 min and 8 min are depicted in Figure 4 and Figure 5, respectively. The x-ray CT images were taken from samples selected by their overall physical appearance as described in Section 3.1 (shown in Figure 2 and Figure 3). For each aggregate shown, the cross section through the middle of the aggregate was selected and presented in Figure 4 and Figure 5. As was mentioned, the solid phases have GSV=0 (black) while the pores have GSV=255 (white). In Figure 4, NV aggregates with three NaOH concentrations were sintered for 4 min. The pore size increased with NaOH concentration. In NV-4%-4min, there are many voids that are interconnected, which is important for the sorption properties of the aggregate. This morphology suggests that the ash particles were not completely molten during the sintering process, and they were loosely bonded. For NV-10%-4min and NV-16%-4min, they have a denser interior structure in comparison to 4 % NaOH with many small pores well distributed. Also, large and round pores were observed along the outer layer of the aggregates. The formation of these large pores can be attributed to degassing of the slag phase in the form of bubbles [36], which escaped from the interior to the surface [14]. Identifying the gaseous products formed during sintering and their sources is an ongoing work. In our previous paper [24], it was found that the surface of NV aggregates attained the high temperature (1160 °C) during sintering, while the core of the aggregate had slightly lower temperature; therefore, the molten phase formed near the surface layer

and was able to entrap the bubbles close to the surface. As the sintering time increased to 8 min (Figure 5), the morphologies are similar to those of 4 min sintering, revealing large and round pores near the surface of the aggregate for NV-10%-8min and NV-16%-8min.

For the WP aggregates (Figure 4 and Figure 5), in general the sizes of the voids and pores are much larger than those in NV aggregates, suggesting that more gas phase was generated during the sintering of this type of coal ash. A possible explanation of this difference is the fact that the liquid phase of the NV aggregates had a higher viscosity in comparison to the liquid phase of the WP aggregates [24].

For WP-4%-4min, a large void was observed in the middle of the aggregate (Figure 4), which is originated from entrapment of gaseous phase by the liquid phase. As reported in our previous study [24], increasing the NaOH concentration in the WP aggregates increases the volume of the liquid phase and lowers the viscosity of the molten phase due to the high calcium content of the WP ash. Accordingly, WP-10%-4min contained entrapped pores near the surface. The entrapped pores in the surface layer for WP-16%-4min are larger than those in WP-10%-4min.

In Figure 5, WP-4%-8min showed a similar morphology as WP-4%-4min; i.e., a large void in the center of the aggregate, while a series of pores were also observed near the surface of the aggregate. Interestingly, increasing the sintering time to 8-min for WP-10 % and 16 % led to entrapment of pores throughout the entire aggregate. This is because the entire aggregate (both the surface and interior) had sufficient time to experience a high temperature (1160 ^{o}C) during sintering [24]. As a result, the molten phase formed in the entire aggregate, so gas bubbles could be entrapped in all parts of the aggregate.

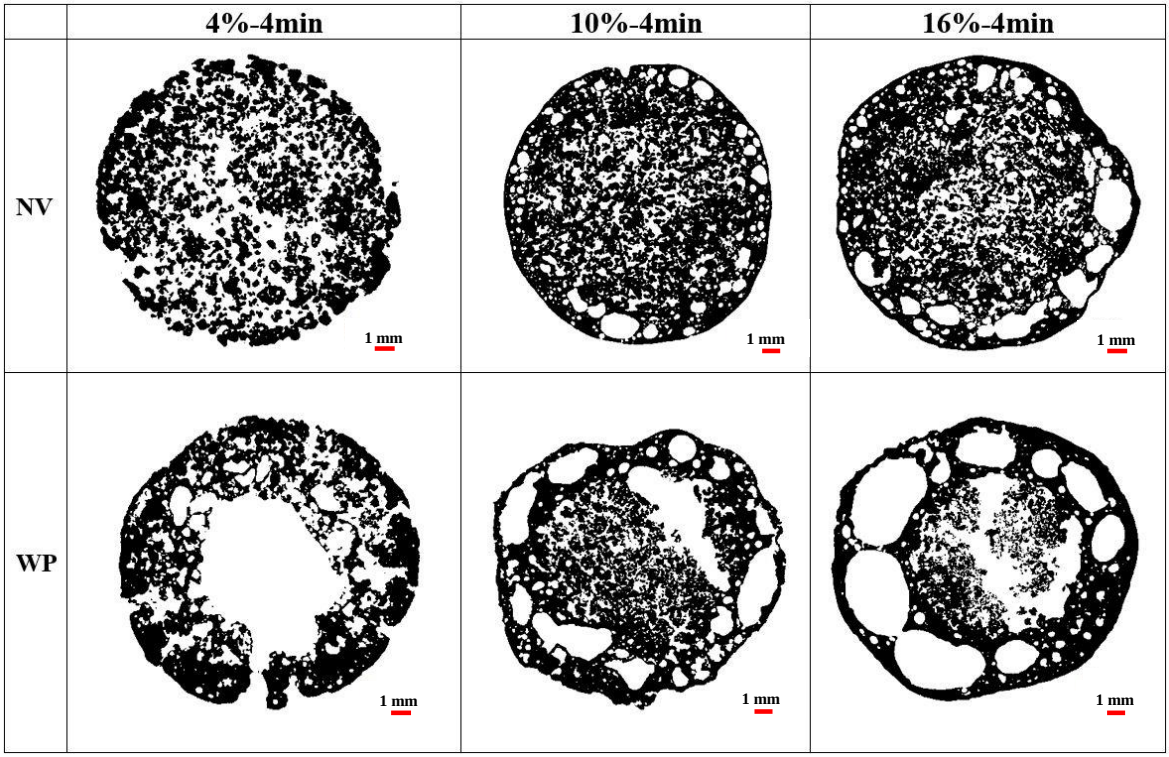

Figure 4. 2-D projections of SPoRA sintered for 4 minutes

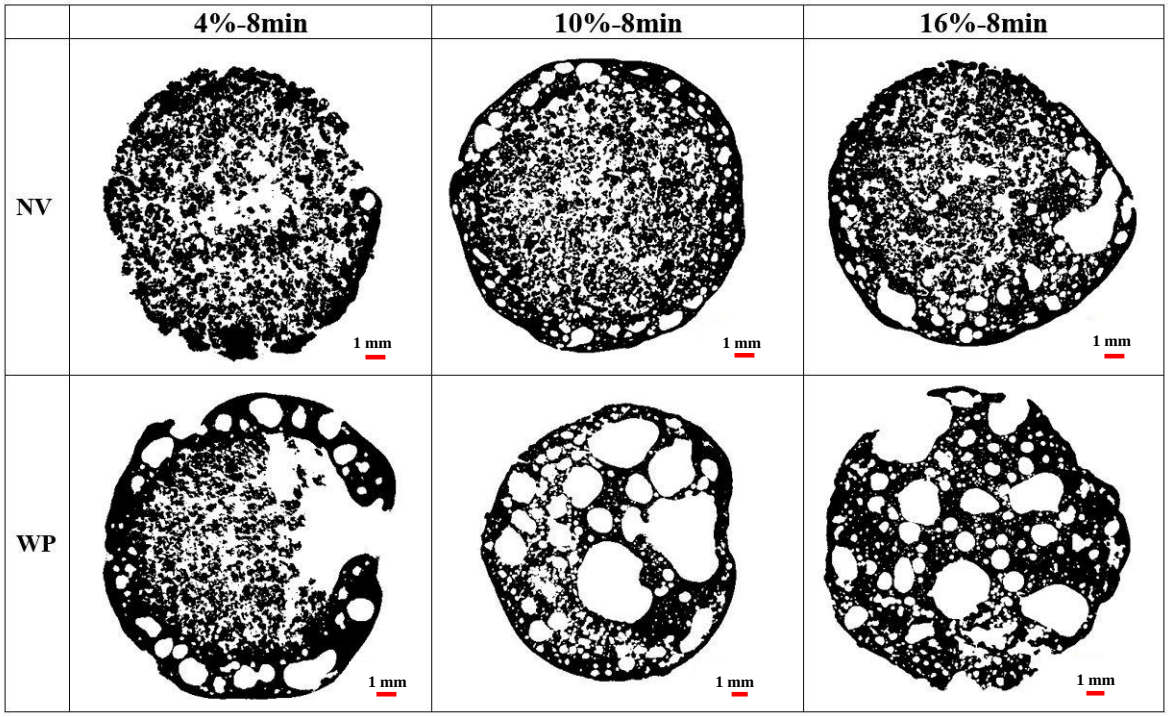

Figure 5. 2-D projections of SPoRA sintered for 8 minutes

3.2.2 Porosity

In order to calculate the porosity of aggregates using XCT results, an aggregate's total cross-sectional area (without considering any of the pores) and area of solids were obtained for each binary image in each 3D data set. By computing the aggregate's total cross-sectional area, adding all the slices together, and using the voxel size, the total volume of each aggregate was obtained. The same procedure was used for the solid area, and by taking the ratio, the porosity was calculated using Equation 2.

$$P = 1 - \frac{Total\ volume\ of\ solids}{Total\ volume\ of\ aggregate} \qquad \text{Equation 2}$$

The porosity of the NV and WP aggregates was also obtained using a buoyancy method according to ASTM C127 [35]. The porosity values calculated using the buoyancy and XCT methods are presented in Figure 6. As can be seen in Figure 6(a), for the NV aggregates, lower values of the porosity were obtained using XCT analysis than those obtained with the buoyancy method, especially at 4 % and 10 % NaOH concentrations. This may be attributed to pores in the NV aggregate that were smaller than about twice the XCT voxel size, 18 µm, and so were not detected by the XCT. Other factors such as testing different samples for buoyancy and XCT, and error in segmentation could lead to the observed difference between porosity measured by buoyancy and XCT. Uncertainties in segmentation also produce uncertainties in porosity of 3.1%. It should be mentioned that for NV-10%-4 min, NV-16%-8 min, WP-10%-8min, and WP-16%-4min, two replicates were analyzed using XCT with coefficients of variation equal to 17.9 %, 10.7 %, 10.4 %, and 8.1 %, respectively, to calculate the porosity uncertainty for the XCT data, and their average

porosity is reported in Figure 6(a). For NV aggregates, a decreasing trend in porosity with increasing NaOH concentration was observed for both XCT and buoyancy test results (Figure 6(b)), while the porosity for WP aggregates remained relatively constant (Figure 6(b)) for all values of NaOH concentration. For the NV aggregates, increasing the sintering time from 4 min to 8 min was found to have negligible influence on the porosity. As shown in Figure 6(a), the porosity values of aggregates at each NaOH concentration sintered for 4 min and 8 min were found to be very similar. Additionally, for the WP aggregates, the fluctuation in the porosity values was found to be within the standard deviation calculated for porosity measurement and accordingly, no specific trend was observed when sintering time varied from 4 min to 8 min. This observation implies further sintering time may only influence the physical appearance of the aggregates (as observed in Figures 2 and 3), but not the porosity.

The porosity of the NV aggregates was found to be higher than the WP aggregates. The porosity varied from 57.8 % to 42.6 % for the NV aggregates, while it was between 48.8 % and 41.6 % for the WP aggregates. Generally, a good agreement between XCT and buoyancy results for WP aggregates was observed. Higher porosity was observed for the WP-10%-8min aggregate in comparison with the WP-10%-4min. This implies that the formation of the liquid phase in the aggregates was successful at this NaOH concentration to entrap the big pores and increase the porosity (see Figure 4 and Figure 5).The high porosity obtained by both techniques showed an excellent capability of both NV and WP SPoRAs for water absorption needed to store a sufficient amount of water for internal curing.

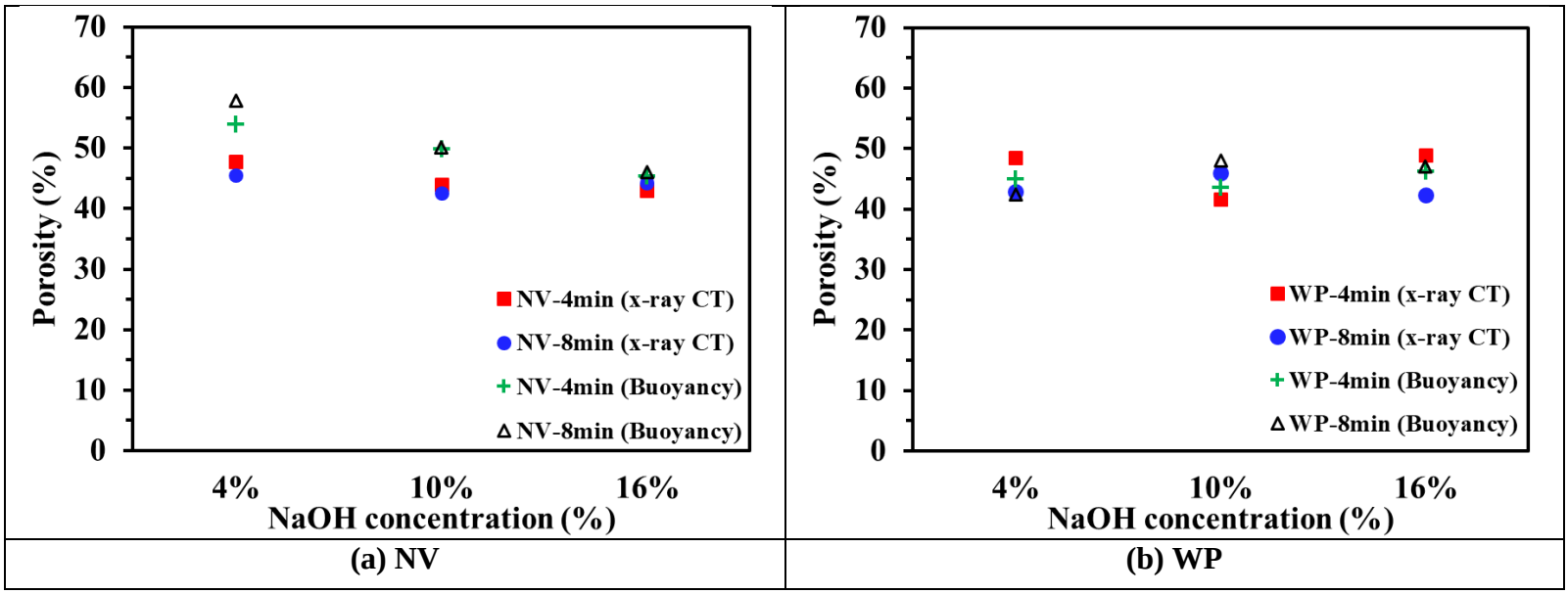

Figure 6. Porosity of aggregates obtained using XCT and buoyancy methods for (a) NV and (b) WP (the maximum standard deviation of porosity measured by buoyancy for three replicates and measured by XCT for two replicates was determined to be 2.59% and 8%, respectively)

3.2.3 Sphericity

It has been reported that spherical aggregates enhance the workability of fresh concrete [37–40], since spheres have a smaller intrinsic viscosity than other shapes. To evaluate the sphericity of the SPoRA, a sphericity index (Ψ), a measure of how close the shape of an aggregate is to a perfect sphere [29,41], was calculated using Equation 3 [41]. To calculate the surface area of the aggregate (A), the perimeter of the aggregate cross section was calculated in all binary images of each data set using the XCT results and then used with the stack of images, along with the voxel size.

$$\psi = \frac{6*V}{D*A} \qquad \text{Equation 3}$$

where:

V = Total volume of aggregate

A = Surface area of aggregate

D = Diameter of a sphere with equal volume to aggregate

D can be calculated using the following equation:

$$D = 2 * \sqrt[3]{\frac{3V}{4\pi}} \qquad \text{Equation 4}$$

The sphericity index was calculated for both the NV and WP SPoRA aggregates for different sintering times. The results are shown in Figure 7 as a function of NaOH concentration. An approximate bilinear behavior was observed for both NV and WP aggregates. NV aggregates retained their sphericity (Ψ=1) with 4 % and 10 % NaOH concentrations sintered for 4 and 8 min and based on Figure 7(a) the onset of deformation was observed after 10 % NaOH concentration. In contrast, WP lost its sphericity (Ψ<1) as the NaOH concentrations passed 4 % and based on the approximate bilinear behavior the onset of deformation would start at 5.85 % NaOH concentration.

To further evaluate the SPoRA sphericity, a threshold value (Ψ_t) was selected for which aggregates were considered to be “close enough” to a perfect sphere. This threshold value was chosen to be the same as the sphericity index of the Platonic dodecahedron shape, which is 0.91 [41]. NV

aggregates were predicted to have sphericity lower than Ψ_t at 13.2 % NaOH concentration, while this same value for WP aggregates was observed to be reached at 10 % NaOH concentration.

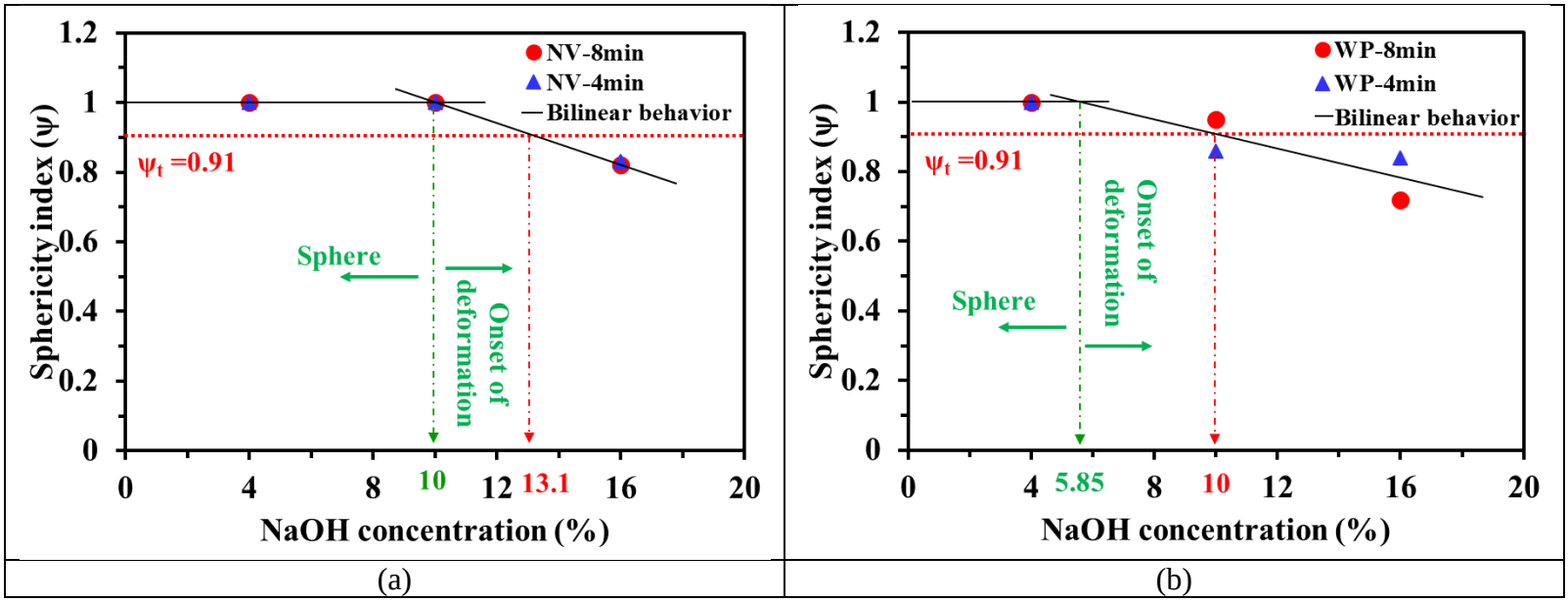

(a) (b)

Figure 7. The sphericity index (Ψ) of (a) NV and (b) WP aggregates (the maximum standard deviation for two replicates was determined to be 0.06)

3.3 Specific gravity

A minimum of three aggregates of each type were tested to obtain representative results for specific gravity measurements. Figure 8 reports the specific gravity for the NV and WP aggregates for both 4 min and 8 min sintering times at 4 %, 10 %, and 16 % NaOH concentrations. For the NV aggregates, it was observed that as the NaOH concentration increased, the specific gravity also slightly increased, which is consistent with the porosity measurements, which decreased with increasing NaOH concentration. It appears that increasing sintering time may not affect the specific gravity significantly as seen in Figure 8(a). For the WP aggregates, the specific gravity

(Figure 8b) of aggregates did not change significantly between different NaOH concentrations although bloating (i.e., formation of gaseous phase and its entrapment inside the aggregate due to formation of liquid phase on the surface of aggregate) occurred for the WP aggregates with large pores forming (as was discussed in Section 3.2.1) in comparison to the NV aggregates. This may be attributed to the fact that the total porosity of both the WP aggregates and the NV aggregates remained relatively similar (Figure 6).

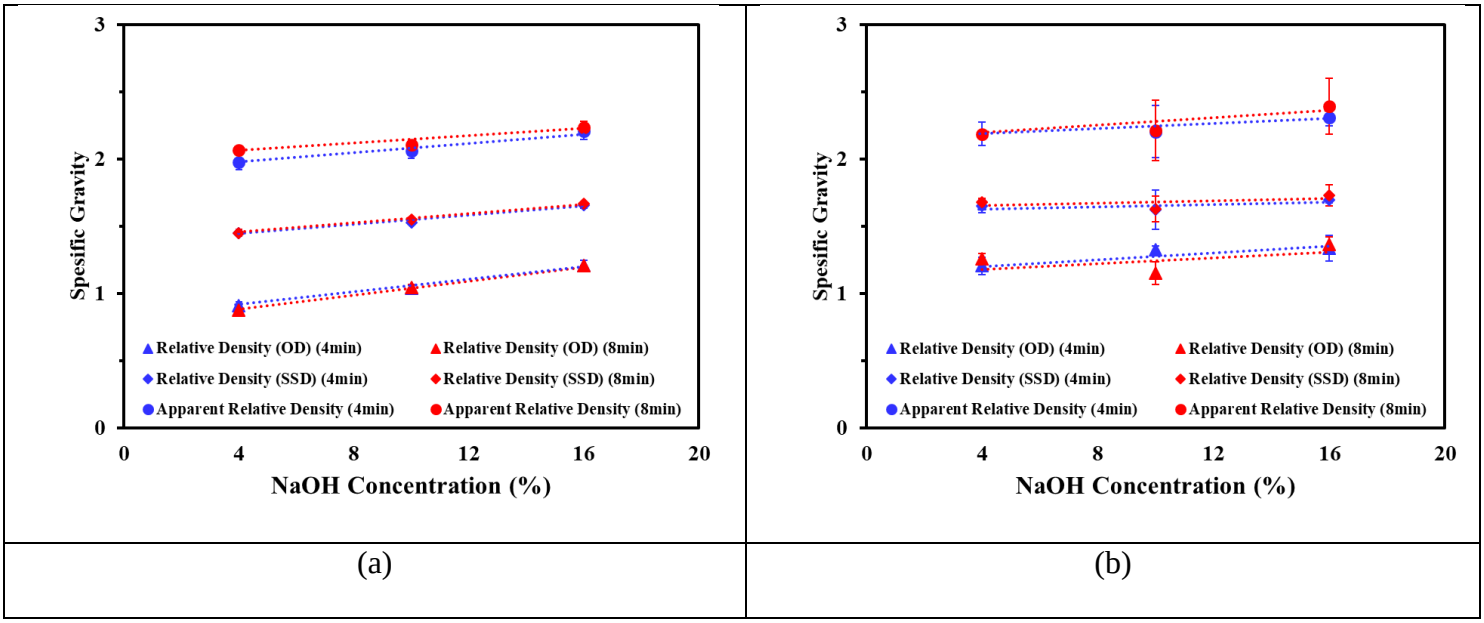

Figure 8. Apparent, oven dry, and saturated surface dry specific gravity of (a) NV sintered for 4min and 8min (b) WP sintered for 4 min and 8 min (the error bars indicate ± one standard deviation for three replicates).

3.4 Water absorption

Since the saturation state of LWA has a direct effect on the internal curing of concrete, the water absorption capacity of aggregates was examined . Figure 9 shows the water absorption of NV and WP

aggregates with different NaOH concentrations and sintering times during the first 120 h of absorption. Rapid absorption was observed over the first 6 h, which is mainly due to the capillary suction of empty capillary pores, and the slower rate of absorbed water after that, so-called secondary absorption, is related to water absorption by larger pores [42]. The experimental results in Figure 9 show that NV and WP SPoRAs have a considerable number of capillary pores, which contributed to rapid water absorption. The rapid absorption suggests a promising potential for using both the NV and WP SPoRA for internal curing.

For the NV aggregates, the water absorption capacity decreased with increasing NaOH concentration, which may be due to reductions in pore volumes as previously observed in Figure 6. However, increasing the sintering time from 4 min to 8 min was found to increase the water absorption capacity for the NV aggregates. This increment may be attributed to the formation of capillary pores that can effectively absorb water.

The water absorption of the WP aggregates was found to be much lower than the water absorption of the NV aggregates, but still within the desired range for internal curing (more than 5 % according to ASTM C1761 [43]). This observation may be attributed to the formation of larger pores in the WP aggregates (see Figure 4 and Figure 5) as opposed to the NV aggregates, which may slow down the water absorption process (needing more time) for the WP aggregates due to a reduction in capillary suction. The formation of larger pores in WP aggregates may be attributed to the higher calcium content in raw WP ash compared with NV ash, which leads to formation of a liquid phase with lower viscosity in the WP aggregates. Consequently, coalescence and pore growth can be easier in the WP aggregates in comparison to NV aggregates (with less calcium) resulting in formation of larger pores. The maximum water absorption of the WP aggregates occurred at 4 % NaOH

concentration sintered for 4 min and 8 min. However, the sintering time and NaOH concentration had less influence on the absorption behavior of the WP aggregates compared to the NV aggregates.

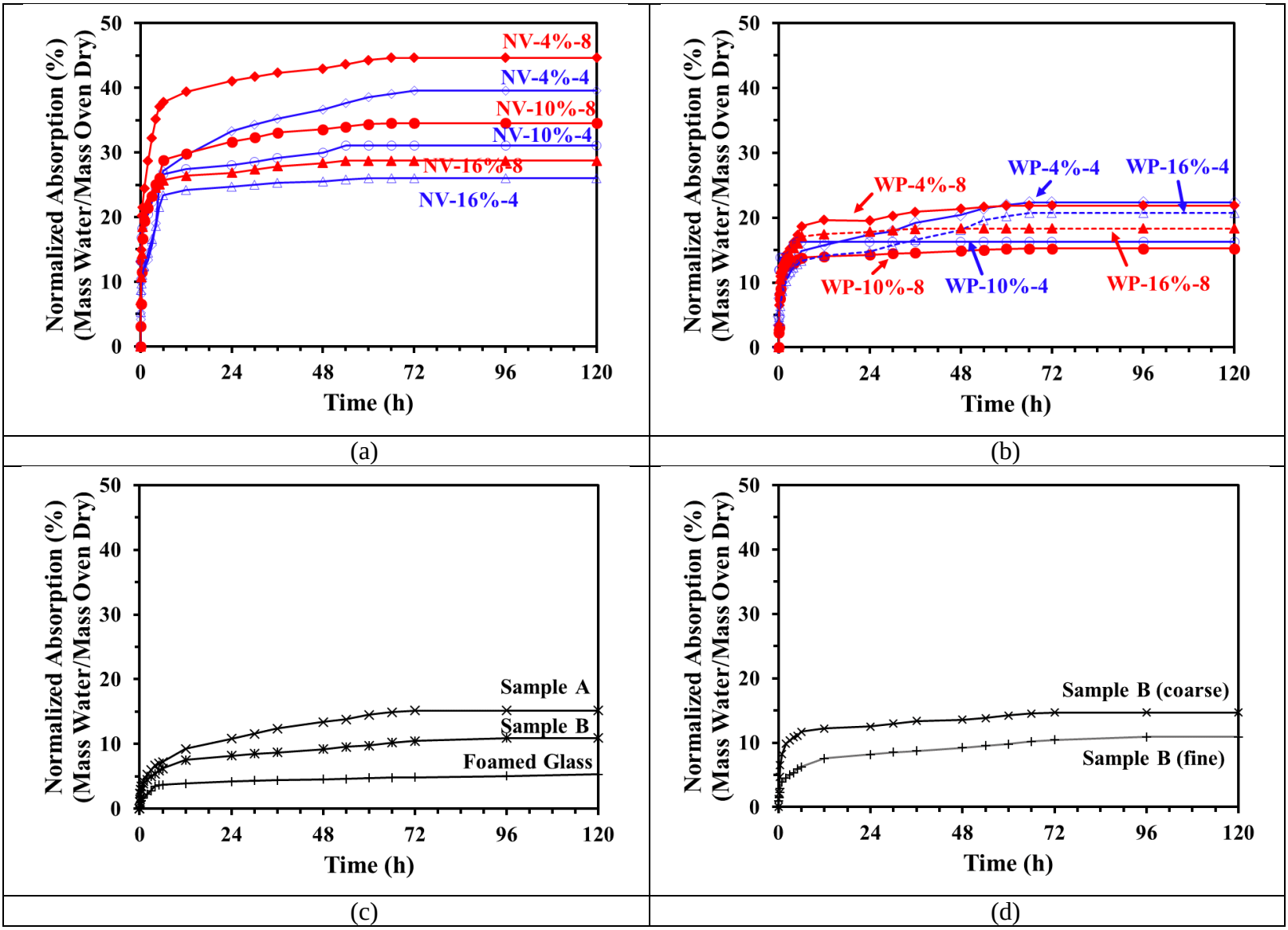

Figure 9. Measured water absorption behavior of different samples as a function of time (a) NV SPoRA (b) WP SPoRA (c) reference LWAs, and (d) coarse and fine Sample B LWA (the maximum standard deviation for three replicates was determined to be 1.5%)

As shown in Figure 9(a) and (b), the 24 h absorption for the SPoRA ranges from 24.7 % to 41 % for NV and from 14.3 % to 19.5 % for WP, which is above the water absorption capacity required

459 by ASTM C1761 [43], i.e., more than 5 %. This value is between 8.1 % and 10.8 % for the reference
460 LWAs (i.e., Sample A and Sample B as shown in Figure 9(c)). As indicated in Figure 9(c), the
461 absorption for foamed glass is less than 5 % even after 72 h, making it less desirable for internal
462 curing. Foamed aggregate contains a disconnected pore structure that hinders water penetration
463 into the pores and limits its water absorption capacity [44]. Both the NV and WP aggregates
464 showed superior absorption capacities in comparison to Sample A and Sample B, which makes
465 the SPoRA promising LWAs to absorb/store sufficient amount of water for concrete internal
466 curing.

467 LWA water absorption behavior also depends on the aggregate size. Larger LWAs generally have
468 larger pores; however, when they are crushed to smaller aggregates, the large pores break down
469 resulting in a reduction in pore volume. Accordingly, the same aggregates with larger particles
470 may have higher water absorption than smaller particles. This was confirmed by comparing the
471 water absorption of coarse and fine Sample B LWA as shown in Figure 9(d) [10]. The coarse
472 Sample B LWA had higher water absorption than did the fine Sample B LWA, but the water
473 absorption of the SPoRA is much higher than even the coarse Sample B LWA.

474 Figure 10 shows a comparison between vacuum absorption and 24 h absorption of the SPoRA.
475 The vacuum absorption shows the maximum possible capacity for absorbing water, while in
476 practice, the 24 h water absorption value is more often used. The difference between vacuum
477 absorption and 24 h absorption, indicated by the gray region in the figure, shows water in pores
478 that cannot be filled during 24 h. These pores need a longer time to be filled due mainly to their
479 larger pore sizes; accordingly, this water is not available for internal curing. The blue region,
480 however, demonstrates the absorption percentage that can be achieved by the capillary suction of
481 pores during the first 24 h. It can be inferred that not all the pores could be filled when the aggregate

was soaked in the water. Holm et al. [44] showed that LWA water absorption is highly dependent on average pore size, pore continuity, and pore size distribution.

For the WP aggregates, the amount of water that is not available for internal curing was found to be higher than for the NV aggregates. This may be due the pore structure of the WP SPoRA as was previously observed in Figure 4 and Figure 5 which showed that WP contains pores with larger sizes than NV. The WP SPoRA aggregates have pores in the range of mm (see Figure 5), and under the soaking condition, it is possible that not all of the pores can absorb water in the first 24 h.

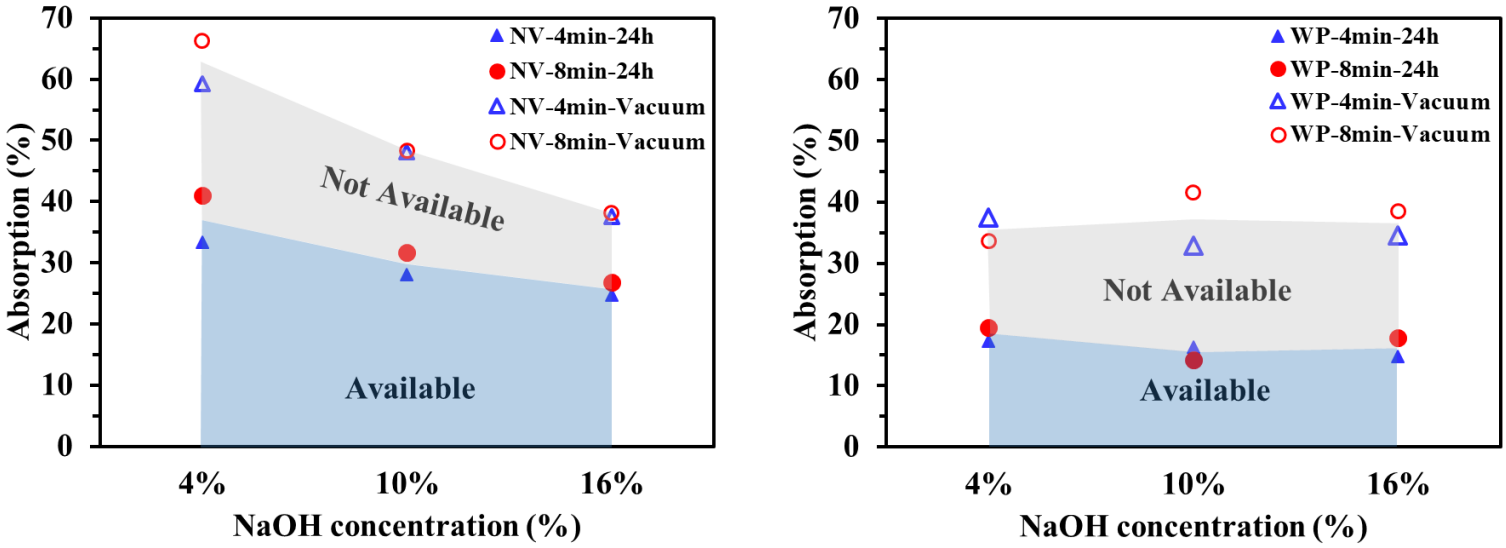

(a) (b)

Figure 10. Vacuum and 72 h water absorption of (a) NV and (b) WP (the maximum standard deviation for three replicates was determined to be 4.5%)

3.5 Water desorption

The desorption isotherm for an LWA that is suitable for concrete internal curing indicates how the LWA can desorb stored water during cement hydration and self-desiccation of concrete to properly cure concrete. The desorption isotherms for the SPoRA after 24 h absorption in water are shown

in Figure 11. 24 h absorption was selected as it is often used in practice to saturate LWAs for internal curing. An efficient LWA shall release more than 85 % of its absorbed water as RH drops to 94 % RH according to ASTM C1761 [43]. Figure 11(a) shows a desorption behavior comparison between an aggregate that is not an efficient LWA for internal curing (schematically drawn and referred to as less efficient LWA) and an LWA that is effective for internal curing (here it is NV-4%-4 min and referred to as efficient LWA). Note that both the efficient and less efficient LWAs have an equal initial water absorption capacity. However, the efficient LWA released more than 90 % of absorbed water at 94 % RH while the less efficient LWA retained a substantial portion of the absorbed water (≈33 % of initial absorbed water) at low RH. The retained water mainly represents water that remains in very small pore sizes (with diameters less than ≈10 nm according to the Kelvin equation [45]) in the LWA. Accordingly, this water is not available for internal curing of concrete since its associated pore diameters are in the range of gel pores in concrete (pores with diameters less than 10 nm [37]). Therefore, its associated capillary suction pressure is above the generated pressure from capillary pores in concrete (pores with diameters less than 10 nm [37]) according to the Kelvin-Young-Laplas equation [46], which prevents its movement for curing from the LWA to the concrete capillary pores during self-desiccation of concrete. References [1,47,48] showed that LWAs that are suitable for concrete internal curing possess pore diameters above 100 nm, and they are efficient in providing water during concrete self-desiccation.

Both the NV and WP aggregates released most of their stored water at RHs above 98 % RH (Figure 11(b) and (c)), which corresponds to pore sizes above 100 nm diameter according to the Kelvin equation [45]. As such, it can be inferred that SPoRA mainly have pores larger than 100 nm, making them suitable for internal curing. Based on Figure 11(b) and (c), the NV and WP aggregates are capable of readily releasing their absorbed water. This also implies that the pore structure of SPoRA is open and well connected, which is supported by the 2-D projections of SPoRA presented

in Figure 4 and Figure 5. As a result, absorbed water can easily move from LWAs to the outside of the aggregate and provide sufficient water for cement hydration during internal curing.

The amount of absorbed water released at 94 % RH is shown in Figure 12. ASTM C1761 indicates 85 % moisture release at 94 % RH as the limit for a suitable aggregate for internal curing. Both the NV and WP SPoRA passed this requirement. Sample A and Sample B LWAs passed the requirement by ASTM C1761, but both of these LWAs have 24 h absorption capacity much less than the SPoRA, as can be seen in Figure 9. Comparing the absorption and desorption behavior of the SPoRA aggregates with the reference LWAs (Figure 9 and Figure 11), it can be concluded that all the SPoRA aggregates studied here are better LWAs for internal curing than are the reference LWAs.

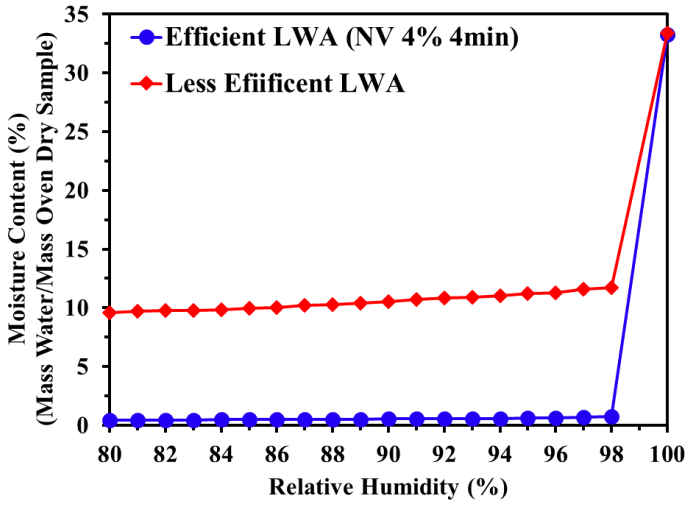

(a)

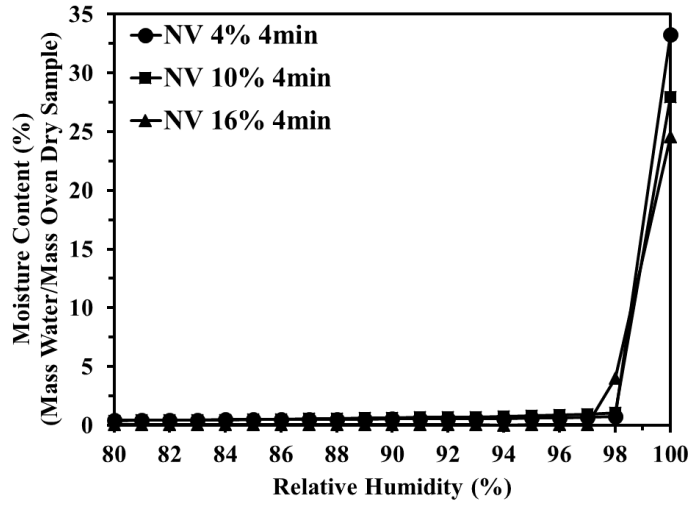

(b)

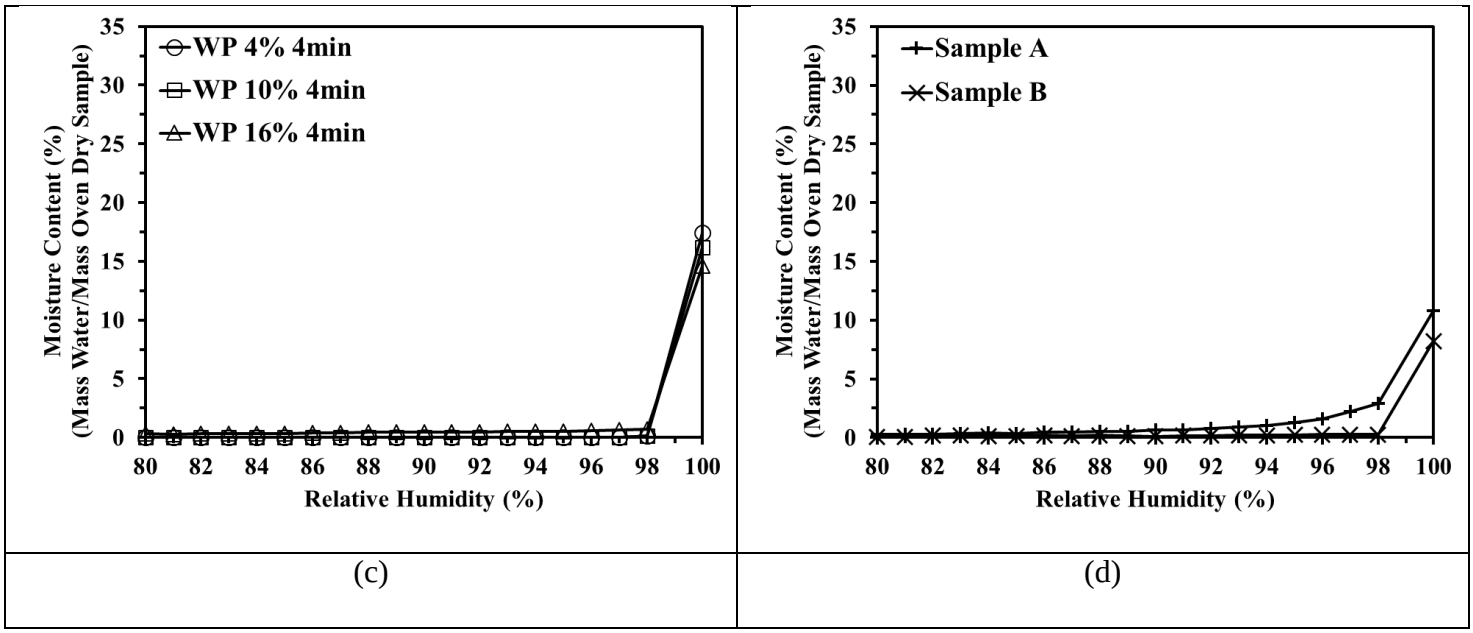

(c) (d)

Figure 11. (a) Example of an efficient and less efficient desorption response, (b) desorption response of NV, (c) desorption response of WP, and (d) desorption response of reference LWAs

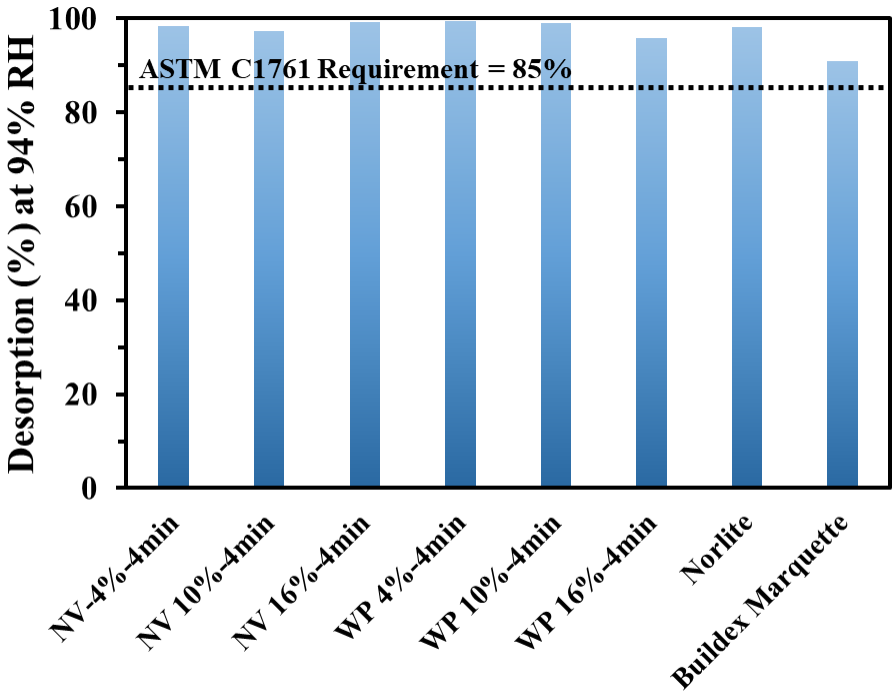

Figure 12. Moisture released at 94 % RH per initial 24 h moisture absorption (%, by mass)

4. Summary and conclusions

This paper examines the potential use of a novel Spherical Porous Reactive Aggregate (SPoRA) as an effective and efficient LWA produced from waste bottom ash for internal curing of concrete. SPoRA possesses three main features that make it a better LWA in comparison to commercial LWAs: a spherical shape to increase the workability of concrete, better sorption properties to absorb and desorb water for internal curing, and a glassy surface with crystalline internal structure to provide surface reactivity with the cementitious matrix while possessing desirable internal crystalline strength [24]. To evaluate the performance of SPoRA for concrete internal curing, its engineering properties, including porosity, sphericity, specific gravity, water absorption, and water desorption were measured.

It was observed that the addition of NaOH at a concentration of 10 % or more can result in non-spherical deformations in the NV aggregates during the sintering process while for the WP aggregates, non-spherical deformation began at a lower NaOH concentration (after 4 %, by mass). This may be because the WP ash has a higher calcium content in comparison to the NV ash, resulting in a higher slag amount during sintering process for WP, which leads to higher deformation for WP in comparison with NV. The NV aggregates maintained the maximum sphericity (i.e., 1) up to 10 % NaOH concentration and had sphericity of 0.82 at 16 % NaOH concentration, while WP aggregates started to lose their maximum sphericity (0.91) before 10 % NaOH concentration.

XCT observations revealed the formation of connected pore structures with sufficient pore spaces for the NV and WP aggregates, favoring their absorption/desorption transport properties. Larger

pores were observed in the WP aggregates compared to the NV aggregates, which may be attributed to a lower viscosity of the liquid phase in the WP aggregates (due to higher calcium content) during sintering than that of the NV aggregates. The lower viscosity allows the production of larger pores as it facilitates expansion of emitted gases formed during the sintering process.

To evaluate the maximum capacity of the SPoRA material for storing water for internal curing, the porosity was measured and a generally good agreement between the porosity measured by XCT and a buoyancy test was observed. Both methods measured the porosity of the SPoRA material to be more than 41.6 % by volume, which is sufficient to store the desired amount of water for internal curing. For the NV aggregates, it was observed that porosity decreased by increasing the NaOH concentration. For the WP aggregates, increasing the NaOH concentration was found to increase the porosity only up to 10 % NaOH concentration, beyond which increasing the NaOH concentration did not seem to significantly affect the aggregate porosity. Increasing the sintering time from 4 min to 8 min was not found to influence the porosity significantly.

An effective LWA should absorb more than 5 % water (by mass) during a 72 h time period and desorb more than 85 % of the absorbed water (by mass) when RH drops to 94 % according to ASTM C1761. Evaluations of the water absorption capacity and the desorption properties of the SPoRA material showed that both the NV and WP aggregates possessed excellent capability in absorbing water, which ranged from 26 % to 44.6 % for NV and from 15.25 % to 22.3 % for WP. Both the NV and WP SPoRA materials showed a superior water absorption capacity in comparison to the reference commercial LWAs (i.e., expanded shale, clay, and slate, or foamed glass). The SPoRA desorption isotherms also showed a superior water desorption capability compared to the reference LWAs. Both the NV and WP aggregates released more than 90 % of absorbed water when RH dropped to 94 %.

This research provides crucial fundamental information (e.g., pore structure, porosity, physical appearance, absorption behavior and desorption behavior) to evaluate whether SPoRA (as a novel LWA from waste bottom ash) has the potential to be used as an effective LWA for concrete internal curing. Based on the results of this study, it can be concluded that SPoRA made using low- and high-calcium waste bottom ashes are effective LWAs that can be used in concrete for the purpose of internal curing. While the specific gravity and porosity measurements obtained in this study can be used as indirect indications of SPoRA mechanical properties, further research is needed to understand the effect of using SPoRA on the mechanical properties of concrete and other concrete properties including shrinkage, freeze-thaw, scaling, elastic modulus, and interfacial transition zone (ITZ) structure.

Acknowledgments

The work presented here has been supported in part by the National Science Foundation (NSF CMMI – 1550723). Any opinions, findings, and conclusions or recommendations expressed in this material are those of the authors and do not necessarily reflect the views of the National Science Foundation.

5. References

[1] S. Ghourchian, M. Wyrzykowski, P. Lura, M. Shekarchi, B. Ahmadi, An investigation on the use of zeolite aggregates for internal curing of concrete, Constr. Build. Mater. 40 (2013) 135–144. doi:10.1016/j.conbuildmat.2012.10.009.

[2] H.K. Kim, H.-K. Lee, Hydration kinetics of high-strength concrete with untreated coal bottom ash for internal curing, Cem. Concr. Compos. 91 (2018) 67–75. doi:10.1016/j.cemconcomp.2018.04.017.

[3] D.P. Bentz, W.J. Weiss, Internal curing: a 2010 state-of-the-art review, US Department of Commerce, National Institute of Standards and Technology, Internal Report #7765, Gaithersburg, Maryland, 2011.

[4] D.P. Bentz, K.A. Snyder, Protected paste volume in concrete: Extension to internal curing using saturated lightweight fine aggregate, Cem. Concr. Res. 29 (1999) 1863–1867.

612 doi:10.1016/S0008-8846(99)00178-7.

613 [5] I. De la Varga, R.P. Spragg, C. Di Bella, J. Castro, D.P. Bentz, J. Weiss, Fluid transport in
614 high volume fly ash mixtures with and without internal curing, Cem. Concr. Compos. 45
615 (2014) 102–110. doi:10.1016/j.cemconcomp.2013.09.017.

616 [6] Y. Wei, Y. Xiang, Q. Zhang, Internal curing efficiency of prewetted LWFAs on concrete
617 humidity and autogenous shrinkage development, J. Mater. Civ. Eng. 26 (2013) 947–954.
618 doi:10.1061/(ASCE)MT.1943-5533.0000883.

619 [7] M. Pour-Ghaz, J. Castro, E.J. Kladivko, J. Weiss, Characterizing lightweight aggregate
620 desorption at high relative humidities using a pressure plate apparatus, J. Mater. Civ. Eng.
621 24 (2011) 961–969. doi:10.1061/(ASCE)MT.1943-5533.0000422.

622 [8] J. Castro, I.D. la Varga, J. Weiss, Using isothermal calorimetry to assess the water
623 absorbed by fine LWA during mixing, J. Mater. Civ. Eng. 24 (2012) 996–1005.
624 doi:10.1061/(ASCE)MT.1943-5533.0000496.

625 [9] R. Henkensiefken, D. Bentz, T. Nantung, J. Weiss, Volume change and cracking in
626 internally cured mixtures made with saturated lightweight aggregate under sealed and
627 unsealed conditions, Cem. Concr. Compos. 31 (2009) 427–437.
628 doi:10.1016/j.cemconcomp.2009.04.003.

629 [10] J. Castro, L. Keiser, M. Golias, J. Weiss, Absorption and desorption properties of fine
630 lightweight aggregate for application to internally cured concrete mixtures, Cem. Concr.
631 Compos. 33 (2011) 1001–1008. doi:10.1016/j.cemconcomp.2011.07.006.

632 [11] M. Dondi, P. Cappelletti, M. D'Amore, R. de Gennaro, S.F. Graziano, A. Langella, M.
633 Raimondo, C. Zanelli, Lightweight aggregates from waste materials: Reappraisal of
634 expansion behavior and prediction schemes for bloating, Constr. Build. Mater. 127 (2016)
635 394–409. doi:10.1016/j.conbuildmat.2016.09.111.

636 [12] O. Arioz, G. Arslan, A. Tuncan, M. Tuncan, G. Kaya, B. Karasu, K. Kilinc, S. Kivrak,
637 Lightweight expanded aggregate production from bottom ash, in: 10th Conf. Exhib. Eur.
638 Ceram. Soc. Berlin, Ger., 2007: pp. 2051–2053.

639 [13] P. Chindaprasirt, C. Jaturapitakkul, W. Chalee, U. Rattanasak, Comparative study on the
640 characteristics of fly ash and bottom ash geopolymers, Waste Manag. 29 (2009) 539–543.
641 doi:10.1016/j.wasman.2008.06.023.

642 [14] M. Aineto, A. Acosta, J.M. Rincon, M. Romero, Thermal expansion of slag and fly ash
643 from coal gasification in IGCC power plant, Fuel. 85 (2006) 2352–2358.

644 [15] R. Vinai, A. Lawane, J.R. Minane, A. Amadou, Coal combustion residues valorisation:
645 Research and development on compressed brick production, Constr. Build. Mater. 40
646 (2013) 1088–1096. doi:10.1016/j.conbuildmat.2012.11.096.

647 [16] M. Balapour, R. Rao, S. Spatari, Y.G. Hsuan, Y. Farnam, Engineering Properties of Fly
648 Ash-Based Lightweight Aggregate, in: World Coal Ash Conf. (WOCA), St. Louis, MO,
649 May 13-16, 2019.

650 [17] C.H. Benson, S. Bradshaw, User Guideline for Coal Bottom Ash and Boiler Slag in Green

651 Infrastructure Construction, User Guidel. Coal Bottom Ash Boil. Slag Green Infrastruct.
652 Constr. 1 (2011) 1–32.

653 [18] J.M.J.M. Bijen, Manufacturing processes of artificial lightweight aggregates from fly ash,
654 Int. J. Cem. Compos. Light. Concr. 8 (1986) 191–199. doi:10.1016/0262-5075(86)90040-
655 0.

656 [19] C.. L. Verma, S.. K. Handa, S.. K. Jain, R.. K. Yadav, Techno-commercial perspective
657 study for sintered fly ash light-weight aggregates in India, Constr. Build. Mater. 12 (1998)
658 341–346. doi:10.1016/S0950-0618(98)00022-1.

659 [20] D. Zorić, D. Lazar, O. Rudić, M. Radeka, J. Ranogajec, H. Hiršenberger, Thermal
660 conductivity of lightweight aggregate based on coal fly ash, J. Therm. Anal. Calorim. 110
661 (2012) 489–495. doi:10.1007/s10973-012-2339-x.

662 [21] S. Bethanis, C.R. Cheeseman, C.J. Sollars, Properties and microstructure of sintered
663 incinerator bottom ash , Ceram. Int. . 28 (2002) 881–886. doi:10.1016/S0272-
664 8842(02)00068-8.

665 [22] C.R. Cheeseman, A. Makinde, S. Bethanis, Properties of lightweight aggregate produced
666 by rapid sintering of incinerator bottom ash, Resour. Conserv. Recycl. 43 (2005) 147–162.
667 doi:10.1016/j.resconrec.2004.05.004.

668 [23] V.G. Karayannis, A.K. Moutsatsou, E.L. Katsika, Sintering lignite fly and bottom ashes
669 via two-step versus conventional process, Sci. Sinter. 48 (2016) 363–370.
670 doi:10.2298/SOS1603363K.

671 [24] P. Billen, M. Mazzotti, L. Pandelaers, N. Ye oo, W. Zhao, Z. Liu, J. Redus, I. Diaz Loya,
672 I. Bartoli, Y. Farnam, S. Spatari, Y.G. Hsuan, Melt ceramics from coal ash: Constitutive
673 product design using thermal and flow properties, Resour. Conserv. Recycl. 132 (2018).
674 doi:10.1016/j.resconrec.2018.01.035.

675 [25] Michelle Torelli, A thermodynamic modeling approach for environmentally optimized
676 prospective design of spherical porous reactive aggregates, Master Thesis, Drexel
677 University, 2019.

678 [26] ASTM D4326-13, Standard Test Method for Major and Minor Elements in Coal and Coke
679 Ash By X-Ray Fluorescence, (2013).

680 [27] W.B. Fuller, S.E. Thompson, The laws of proportioning concrete, Trans. Am. Soc. Civ.
681 Eng. 33 (1907) 222–298.

682 [28] F.H. Kim, S.P. Moylan, E.J. Garboczi, J.A. Slotwinski, Investigation of pore structure in
683 cobalt chrome additively manufactured parts using X-ray computed tomography and
684 three-dimensional image analysis, Addit. Manuf. 17 (2017) 23–38.
685 doi:10.1016/j.addma.2017.06.011.

686 [29] J.W. Bullard, E.J. Garboczi, Defining shape measures for 3D star-shaped particles:
687 sphericity, roundness, and dimensions, Powder Technol. 249 (2013) 241–252.
688 doi:10.1016/j.powtec.2013.08.015.

689 [30] Y. Shields, E. Garboczi, J. Weiss, Y. Farnam, Freeze-thaw crack determination in

cementitious materials using 3D X-ray computed tomography and acoustic emission, Cem. Concr. Compos. 89 (2018) 120–129. doi:10.1016/j.cemconcomp.2018.03.004.

[31] E. Masad, V.K. Jandhyala, N. Dasgupta, N. Somadevan, N. Shashidhar, Characterization of Air Void Distribution in Asphalt Mixes using X-ray Computed Tomography, J. Mater. Civ. Eng. 14 (2002) 122–129. doi:10.1061/(ASCE)0899-1561(2002)14:2(122).

[32] R.D. Hanna, R.A. Ketcham, X-ray computed tomography of planetary materials: A primer and review of recent studies, Chemie Der Erde - Geochemistry. 77 (2017) 547–572. doi:10.1016/j.chemer.2017.01.006.

[33] M. Cybernetics, Image-Pro Plus 6.0, (2003).

[34] M.A.B. Promentilla, T. Sugiyama, T. Hitomi, N. Takeda, Quantification of tortuosity in hardened cement pastes using synchrotron-based X-ray computed microtomography, Cem. Concr. Res. 39 (2009) 548–557. doi:10.1016/J.CEMCONRES.2009.03.005.

[35] ASTM Subcommittee C09.20, C0127 - Standard Test Method for Relative Density (Specific Gravity) and Absorption of Coarse Aggregate, ASTM Int. (2015) 5. doi:10.1520/C0127-15.2.

[36] M. Aineto, A. Acosta, J.M. Rincón, M. Romero, Production of lightweight aggregates from coal gasification fly ash and slag, World Coal Ash. (2005) 11–15.

[37] P. Monteiro, Concrete: microstructure, properties, and materials, McGraw-Hill Publishing, 2006.

[38] M. Kikuchi, T. Miura, Y. Dosho, M. Narikawa, Application of recycled aggregate concrete for structural concrete. Part 1–experimental study on the quality of recycled aggregate and recycled aggregate concrete, in: Sustain. Constr. Use Recycl. Concr. Aggreg. Proc. Int. Symp. Organised by Concr. Technol. Unit, Univ. Dundee Held Dep. Trade Ind. Conf. Centre, London, UK 11–1, Thomas Telford Publishing, 1998: pp. 55–68.

[39] D. Matias, J. De Brito, A. Rosa, D. Pedro, Mechanical properties of concrete produced with recycled coarse aggregates–Influence of the use of superplasticizers, Constr. Build. Mater. 44 (2013) 101–109. doi:10.1016/j.conbuildmat.2013.03.011.

[40] J.F. Douglas, E.J. Garboczi, Intrinsic viscosity and the polarizability of particles having a wide range of shapes, Adv. Chem. Phys. 91 (1995) 85–154.

[41] H. Wadell, Volume, shape, and roundness of rock particles, J. Geol. 40 (1932) 443–451.

[42] ASTM Standard C1585, Standard Test Method for Measurement of Rate of Absorption of Water by Hydraulic Cement Concretes, ASTM Int. 41 (2013) 1–6. doi:10.1520/C1585-13.2.

[43] ASTM, Standard specification for lightweight aggregate for internal curing of concrete, C1761. (2015) West Conshohocken, PA. doi:10.1520/C1761.

[44] T.A. Holm, O.S. Ooi, T.W. Bremner, Moisture dynamics in lightweight aggregate and concrete, in: Theodore Bremner Symp. High-Performance Light. Concr., 2003: pp. 167–184.

[45] A. Radlinska, F. Rajabipour, B. Bucher, R. Henkensiefken, G. Sant, J. Weiss, Shrinkage mitigation strategies in cementitious systems: A closer look at differences in sealed and unsealed behavior, Transp. Res. Rec. 2070 (2008) 59–67. doi:10.3141/2070-08.

[46] H.S. Esmaeeli, Y. Farnam, D.P. Bentz, P.D. Zavattieri, W.J. Weiss, Numerical simulation of the freeze–thaw behavior of mortar containing deicing salt solution, Mater. Struct. 50 (2017) 96. doi:10.1617/s11527-016-0964-8.

[47] O.M. Jensen, P. Lura, Techniques and materials for internal water curing of concrete, Mater. Struct. 39 (2006) 817–825. doi:10.1617/s11527-006-9136-6.

[48] J.H. Kim, S.W. Choi, K.M. Lee, Y.C. Choi, Influence of internal curing on the pore size distribution of high strength concrete, Constr. Build. Mater. 192 (2018) 50–57. doi:10.1016/j.conbuildmat.2018.10.130.